ORIGINAL ARTICLE



A single camera unit-based three-dimensional surface imaging technique

Yinhe Wang¹ · Xiangyu Guo¹ · Jungsub Kim¹ · Pengfei Lin¹ · Kuan Lu¹ · Hyunjae Lee¹ · ChaBum Lee¹

Received: 28 February 2023 / Accepted: 28 June 2023 © The Author(s), under exclusive licence to Springer-Verlag London Ltd., part of Springer Nature 2023

Abstract

This paper introduces a simple three-dimensional (3D) stereoscopic method using a single unit of an imaging device consisting of a charge-coupled device (CCD) and a zoom lens. Unlike conventional stereoscopy, which requires a pair of imaging devices, 3D surface imaging is achieved by 3D image reconstruction of two images obtained from two different camera positions by scanning. The experiments were performed by obtaining two images of the measurement target in two different ways: (1) by moving the object while the imaging device is stationary, and (2) by moving the imaging device while the object is stationary. Conventional stereoscopy is limited by disparity errors in 3D image reconstruction because a pair of imaging devices is not ideally identical and alignment errors are always present in the imaging system setup. The proposed method significantly reduced the disparity error in 3D image reconstruction, and the calibration process of the imaging system became simple and convenient. The proposed imaging system showed a disparity error of 0.26 in the camera pixel.

Keywords Stereoscopy · 3D imaging · Surface Metrology · Disparity · Calibration

1 Introduction

3D shape acquisition can be divided into contact and non-contact techniques [1]. Contact techniques have been used in the industry for a long time. Contact techniques have been used in the industry earlier. The advantage of contact measurement is high measurement accuracy, which is suitable for the precision of the three structural parameters of small workpieces, and its precision can reach the nanometer level [2, 3]. However, contact measurement is severely limited by the shape of the measuring tool and the target to be measured. The fatal flaw of these techniques is that they run the risk of damaging the test sample, especially when measuring non-rigid bodies [4].

Non-contact surface metrology is gaining popularity in a variety of markets to overcome the limitations of contact measurement. The advantage of non-contact techniques is the speed of measurement, which typically measures areas

Published online: 03 July 2023

rather than single points on a target [5]. An overview of the above techniques is summarized in Fig. 1.

Three-dimensional (3D) surface imaging as a non-contact surface measurement method is becoming popular in a variety of market segments, such as virtual reality, measurement and inspection, manufacturing, medical diagnosis, video game entertainment, and so on [6–9]. With the development of high-resolution and high-speed imaging systems along with powerful computational algorithms [10, 11], 3D imaging technology can be adapted to numerous applications in many ways by combining various 3D surface imaging schemes and powerful software technology including artificial intelligence. Over the past few decades, numerous 3D surface imaging techniques have been introduced. Some classic passive measurements include, but are not limited to, stereoscopy [12, 13] and strobe stereoscopy [14-16]. And some active measurement techniques commercially available in the industry may include Structured Light 3D scanning [17–19], time-of-flight scanning [20–22], interferometry [23], holographic imaging [24], and so on.

The above-mentioned 3D surface imaging techniques have their own peculiarities in terms of application. Stereoscopy is the most widely used multi-camera technology due to its low cost and compact configuration [25, 26], stereoscopy calculates thickness information based on the concept of epipolar



ChaBum Lee cblee@tamu.edu

J. Mike Walker '66 Department of Mechanical Engineering, Texas A&M University, 3123 TAMU, College Station, TX 77843, USA

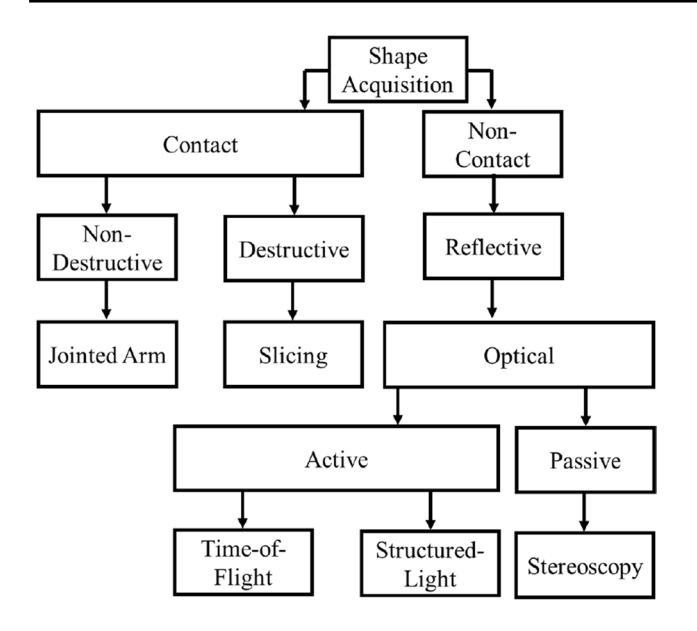
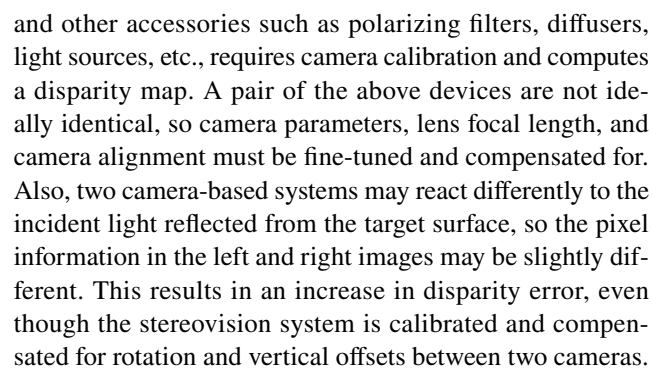


Fig. 1 Summary of 3D shape acquisition techniques

geometry. Since the intrinsic and extrinsic parameters of both imaging devices are known. By finding the target position in different images, the distance of the object from the camera can be determined by triangulation [27]. The stereoscopic system relies entirely on computer vision algorithms to achieve 3D reconstruction. However, it is limited to measuring nontextured (smooth) 3D surface features, since no difference in pixel intensities between the left and right images will cause the 3D image reconstruction to fail. Guo et al. recently introduced strobe stereoscopy, which combines stereoscopy and stroboscopy for in-process 3D surface imaging of the rotating target, but it is also limited to measuring non-textured parts [14–16]. The structured light scanning method uses time-varying and spatial frequency modulated fringe patterns incident on the target surface. However, this method is highly dependent on the performance of the camera and fringe pattern generator and is limited to a short measurement range. The time-of-flight method captures the target image at short to long ranges and calculates the difference in transit time between the incident and reflected light pulses. It has been widely used for military scanning [28] or light detection and ranging (LiDAR) in autonomous vehicles [29]. However, this method offers lower resolution than stroboscopy and structured light scanning methods, is sensitive to lighting conditions, and the system is difficult to calibrate. Interferometry and holographic imaging systems are often used to measure high-precision 3D profiles of optical surfaces but offer very short range measurements and are expensive.

In this study, a new stereovision scheme was proposed. Conventional stereoscopy, which uses a pair of imaging devices (e.g., charge-coupled device (CCD) or complementary metal-oxide semiconductor (CMOS)), imaging lenses,



To avoid such alignment, calibration, and disparity error issues in conventional stereoscopy, a single-camera system-based stereoscopy was proposed in this study. Unlike conventional stereoscopy, which requires a pair of imaging devices, 3D surface imaging was achieved by 3D image reconstruction of two images obtained from two different camera positions. The proposed imaging and calibration procedures are discussed below and compared with those of conventional stereoscopy.

2 Measurement method

Through the movement of the target or imaging devices, two images of the target at different locations are obtained by scanning. Then the 3D surface image can be reconstructed using the stereoscopy algorithm.

2.1 Stereoscopic imaging system

The conventional stereoscopic technique is implemented using a pair of imaging devices to acquire multi-view images of the target at different locations. The process of triangulation used in stereoscopy is based on epipolar geometry. Epipolar geometry is the description of the geometric relationships between two different perspective views of the same 3D scene. The schematic methodology of stereoscopic measurement is shown in Fig. 2. The coordinates of an object point G in the global SRS (Spatial Reference System) are (X_G, Y_G, Z_G) , and the point is projected on the image plane of the left and right imaging devices, respectively. In the left imaging device SRS, the coordinates of the projection point P_l are (X_{pl}, Y_{pl}) and the projection point P_r in the right imaging device SRS are (X_{pr}, Y_{pr}) . Those points lie on the same epipolar line, and the relation can be calculated using the disparity.

In the schematic above, z is the distance from the target to the imaging device, f is the effective focal length of the imaging device, and B is the baseline between a pair of imaging devices.



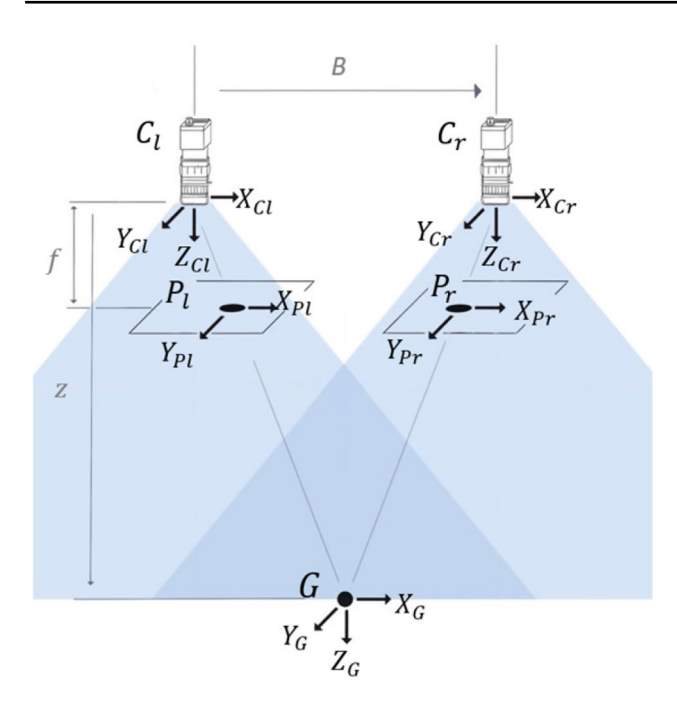


Fig. 2 The principle of conventional stereoscopy

Based on the principle of projective geometry, the disparity between two images and the depth of the target can be calculated as:

$$z = \frac{Bf}{x_{Pr} - x_{Pl}} \tag{1}$$

Where $x_{Pr} - x_{Pl}$ is the disparity between two images.

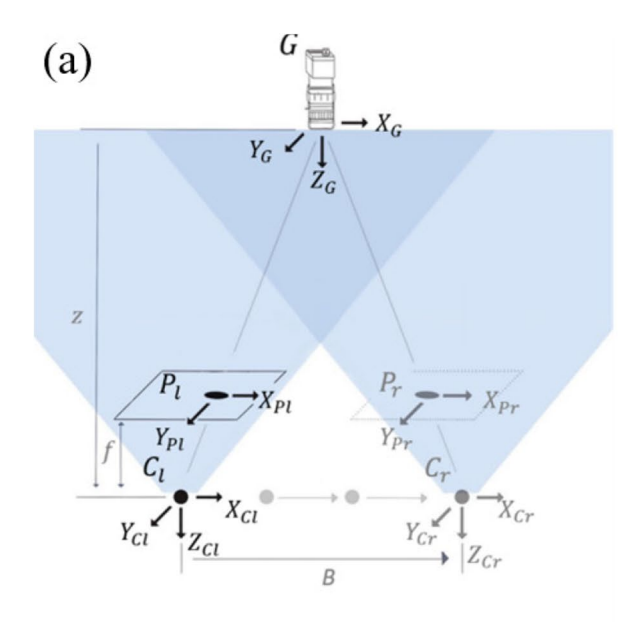


Fig. 3 The proposed stereoscopy: (a) Method #1 and (b) Method #2

The global SRS of the detected object point G is calculated as follows:

$$X_G = \frac{x_{Pl}z}{f} \tag{2}$$

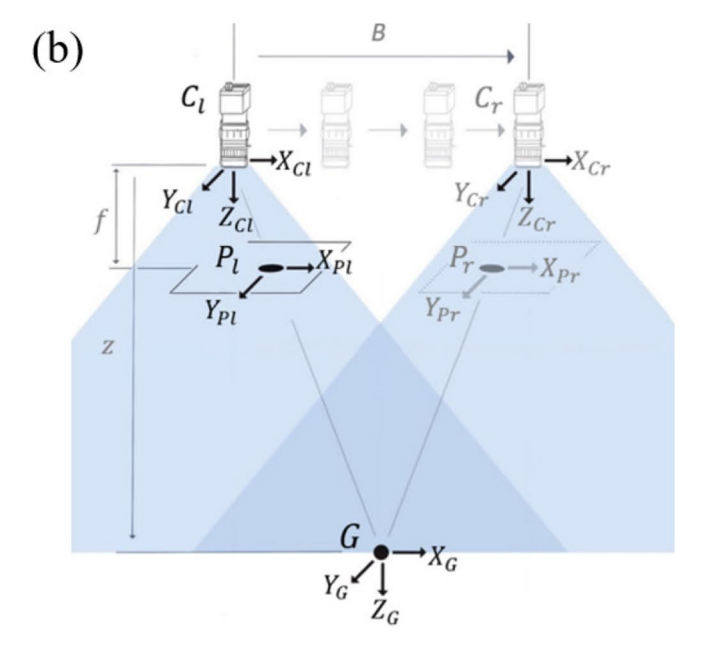
$$Y_G = \frac{y_{Pl}z}{f} \tag{3}$$

2.2 Single camera unit-based 3D surface imaging technique

Based on the 3D image reconstruction principle described above, an image taken at a single position cannot generate disparity, however, the disparity can be calculated by adjusting the relative position of the imaging device or the target, since the parameter obtained from two views is sufficient for triangulation and 3D image reconstruction. Using the geometric transformation described in Fig. 3, a virtual imaging device can be made equivalent. The virtual imaging device at C_r shares the same corrected calibration matrix ($K_l = K_r$) as the physical imaging device C_l . The corrected calibration matrix (K) considering the non-square and non-perpendicular aspect of the pixels and the calibration matrix is shown below:

$$K = \begin{bmatrix} fm_x & s & c_x \\ 0 & fm_y & c_y \\ 0 & 0 & 1 \end{bmatrix}$$
 (4)

Where skew parameter $s = fcos(\alpha)$ introduces this correction, α being the angle between two sides of the pixel. And





 m_x and m_y represent the number of pixels per length unit along the X-axis and Y-axis. The values of c_x and c_y correspond to the optical center coordinates in pixels at the lower left corner of the sensor.

This calibration process is relatively simple and fast compared to conventional stereoscopic techniques. This is because, in the conventional method, the intrinsic parameters of each imaging device (K_l and K_r) require independent calibration.

The stereoscopic technique can achieve accurate 3D reconstruction with high speed and superior stereo matching ability. Conventional stereoscopy requires two imaging devices with precisely calibrated internal and external parameters. In some industrial scenarios, the space is too limited to accommodate a pair of imaging devices, and the system alignment is greatly affected by environmental factors. In this theory, a novel 3D reconstruction method is proposed where only a single imaging device is used for stereo vision. Two experiments were designed to evaluate the proposed methods.

In method #1, the setup is shown in Fig. 3a. The imaging device is stationary, and the target motion is in a horizontal direction. Two images of the target were captured from different perspectives ($C_L \& C_R$). On the other hand, in method #2 as depicted in Fig. 3b, the target is stationary, and the imaging device motion is in a horizontal direction. Two images of the target were captured from different perspectives ($C_L \& C_R$).

3 Experiments

3.1 Experimental system

To evaluate the performance of the single camera unit-based 3D imaging technique, two independent vision systems

were built under laboratory conditions. The configuration of method #1 is illustrated in Fig. 4a. The camera was mounted on a table clamp attached to an optical breadboard, and the precision linear stage controlled by a stepper motor was used to move the target for scanning. On the other hand, in method #2, as shown in Fig. 4b, the target was mounted on an optical table and a UFACTORY xArm 6 Collaborative Robot was used to move the camera for scanning. The robotic system has a repeatability of ± 0.1 mm.

For verification purposes, a CCD laser displacement sensor-based measurement system was constructed to measure the thickness of the specimen shown in Fig. 5. A Keyence LK-G35 laser displacement sensor with 50 nm repeatability was mounted on an optical stage. The sample was placed on a Trilogy single-axis linear stage (0.1 μ m accuracy). The line scan data of the target thickness was set as the reference value.

All experimental configurations use the same imaging device, the Basler acA5472-17 CCD camera, to acquire images. The camera is a CMOS with a sensor size of 13.1 mm \times 13.1 mm and a resolution of 5472 pixels \times 3648 pixels; the pixel size of the imaging system is 2.4 $\mu m \times 2.4$ μm . The camera is equipped with a Moritex ML-U1217SR-18C lens with a focal length of 12 mm. The imaging system includes an illumination device with a ring-shaped LED. The data were processed in the MATLAB and LABVIEW environments.

3.2 Calibration

Calibration is an essential step in determining the internal and external parameters of the camera, the accuracy of which dramatically affects the quality of the 3D reconstruction [30]. An aluminum oxide calibration checkerboard with a square side length of 0.5 mm and an accuracy of ± 20 um was used as the calibration target, as shown in Fig. 6.

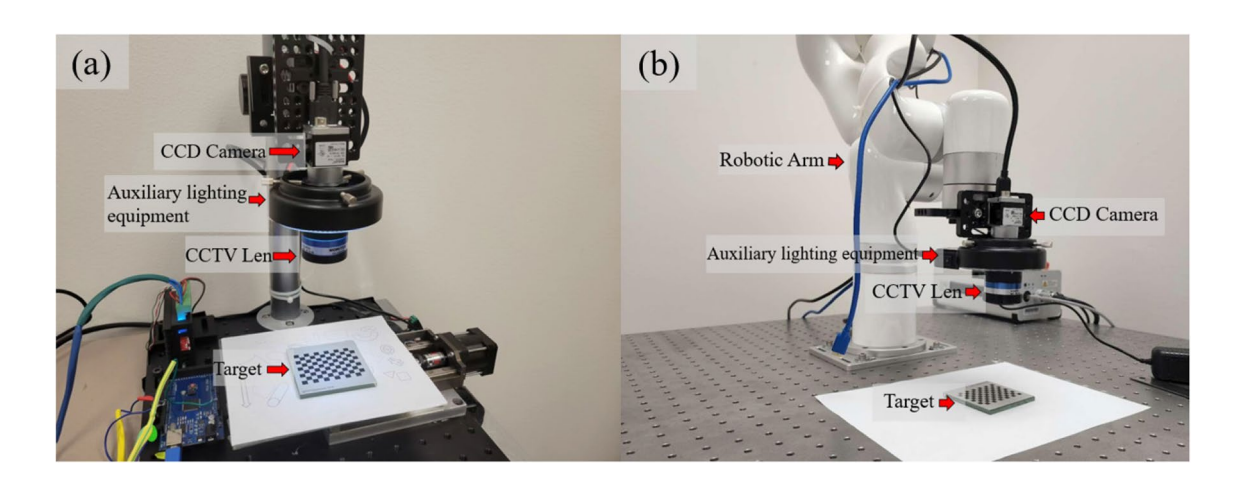


Fig. 4 Experimental setup: (a) Method #1 and (b) Method #2



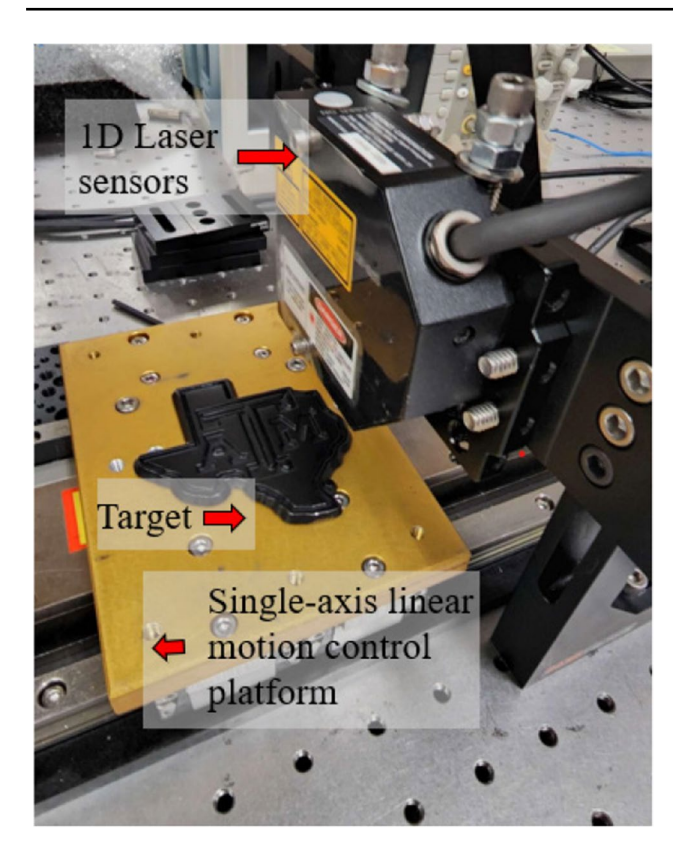


Fig. 5 Displacement sensing system

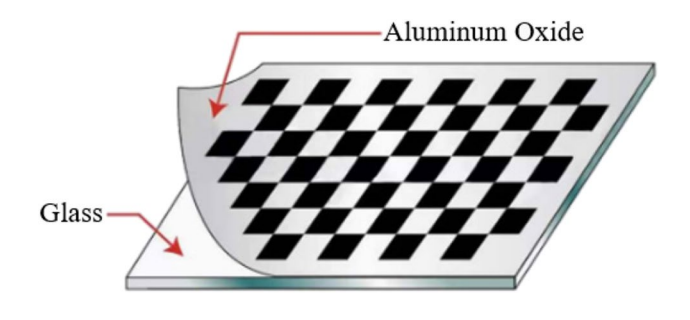


Fig. 6 The material property of the GP070 calibration checkerboard

Based on the principle in Section 2.2, two images of the calibration target can be captured by the camera during target or camera movement. 50 groups of checkerboard images were taken at different positions for system calibration, as shown in Fig. 7. For a single camera system, camera #2 has the same parameters as camera #1 because it is an equivalent camera that does not physically exist. The calibration procedure of method #1 discussed in Section 2.2 was applied. For the camera calibration, the Stereo Camera Calibrator application in MATLAB was used, which adopted Zhang's calibration algorithm [31].

The histogram of reprojection errors for method #1, method #2, and conventional is shown in Fig. 8, and the calibration results of the camera system are shown in Table 1. Additionally, the calibration results provide the camera coordinate data, and it shows within 0.5mm error compared to the real camera coordinate.

3.3 Image acquisition

3.3.1 Experiment: Method #1

In the first experiment, the setup Arduino IDE sends the digital signal to the stepper motor controller to scan the sample target. The target is placed in the center of the camera's field of view. We installed a cross laser emitter behind the camera to adjust its alignment on the target by specular projection. In a pair of images, the first image was taken when the stage moved -4.0 mm and the second image was taken when the stage moved in the opposite direction to +4.0 mm.

3.3.2 Experiment: Method #2

Instead of moving the target, the camera was moved in the Method #2 experiment. The camera was attached to the end effector of a robotic arm whose motion was controlled by a Python-coded program. As in method #1, a pair of images was taken, the first when the camera was moved -4.0 mm

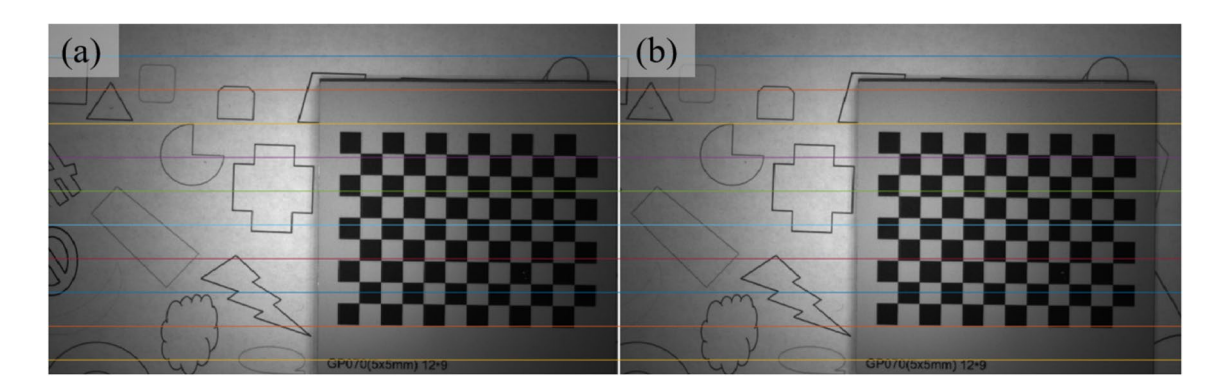


Fig. 7 A pair of checkerboard images for camera calibration: (a) left location and (b) right location

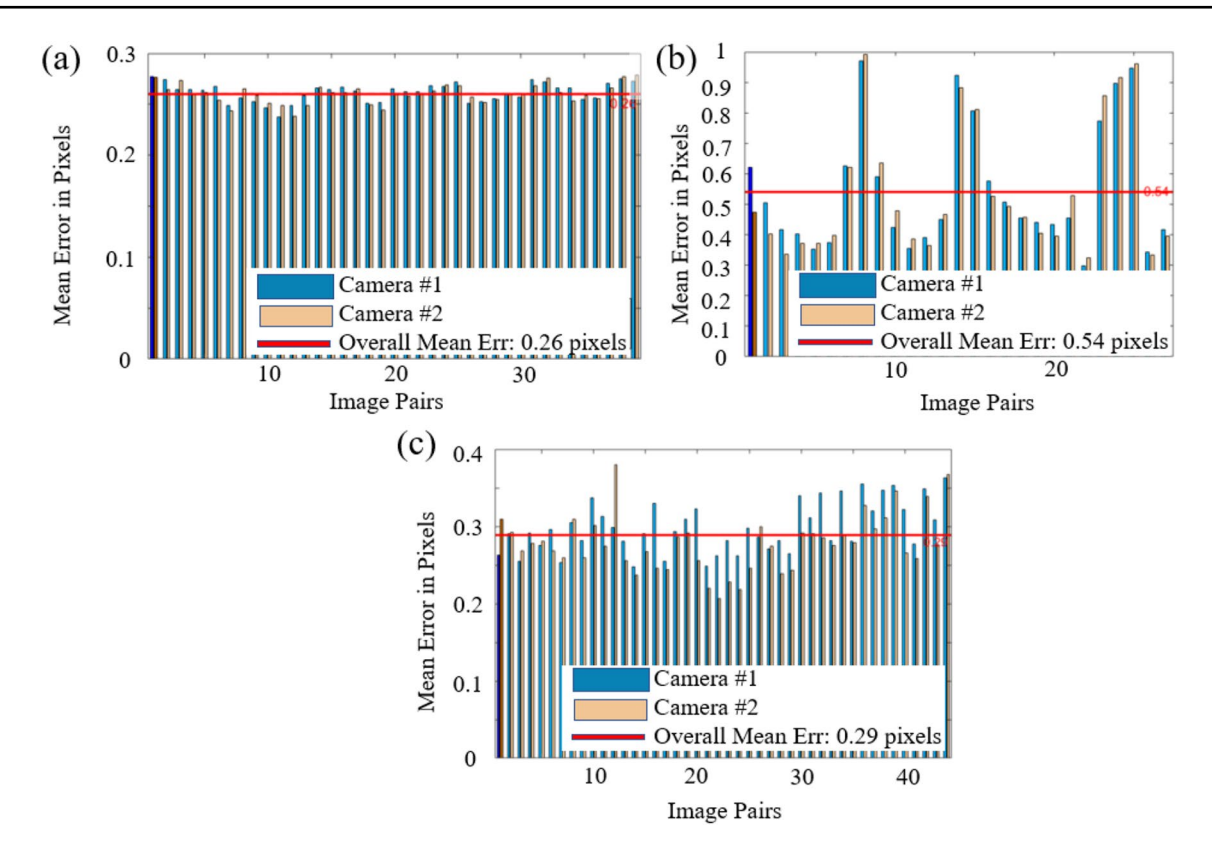


Fig. 8 Reprojection Error Histogram: (a) Method #1, (b) Method #2, and (c) Conventional Method

Table 1 Comparison of Reprojection Errors of Two Proposed Methods and Conventional Methods

	Method #1	Method #2	Conventional method
Reprojection Error (pixel)	0.26	0.54	0.29

and the second when the camera was moved to +4.0 mm. The SRS of the camera can be calculated by matrix transformation, and the external parameters of the system can be obtained.

3.4 Depth data processing

The result of 3D image reconstruction is directly affected by the quality of the raw image captured by the camera. The reflections, shadows, electromagnetic interference, and other factors can cause noise in the 3D data, which affects the quality and accuracy of the depth calculation. To improve the 3D reconstruction result, these unwanted noises must be suppressed by filter processing. The image processing is achieved by the following steps: (1) Extract depth data, (2) Separate the target and background, (3) Calculate the mean value of the background thickness, (4) Remove the

mean value from both the target and background, (5) Filter the target and background separately, (6) Overlay the target and background to generate processed depth data, (7) Reconstruct the 3D surface image. The process flowcharts are shown in Fig. 9.

The pairing of pixels in two images is critical to the disparity calculation. For objects without surface features, the mismatch is easy to occur, resulting in a significant error in disparity computation. In this study, a unique background design was introduced to reduce the disparity error. The background is mainly white and filled with irregular geometric patterns (Fig. 10b). When the target lacks surface features, the algorithm can pick up feature points in the background that can be used for matching. This unique texture design can reduce the feature point matching error in low-texture images, thereby reducing the disparity computation error.

The edge detection algorithm was used to separate the target from the background. It is possible to have a deviation of a few pixels in edge detection, which may cause some background points to be classified as the target, or the target to appear as the background. This could cause a significant error in the depth calculation at the edge. In this paper, after the target edge is detected, as shown in the red circle in Fig. 10c, the mask of the target is



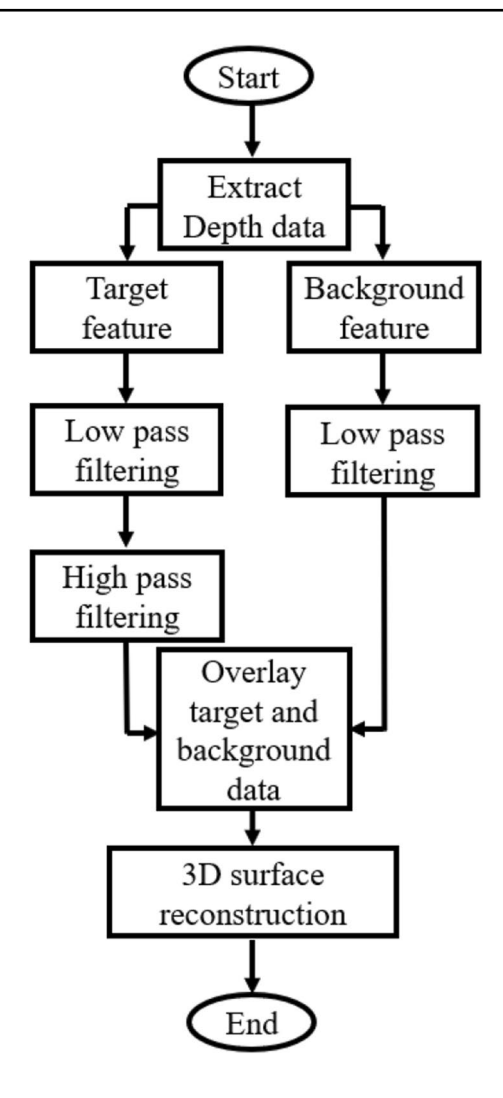


Fig. 9 3D Image Reconstruction Process Flowchart

obtained by reducing 10 pixels from the edge. As shown in the green circle in Fig. 10d, the background mask is obtained by expanding 10 pixels based on the edge shown in the blue circle in Fig. 10e.

To evaluate the performance of the thickness estimation, a linear measurement was performed horizontally along the center of the circle (Fig. 10g). The comparison of raw and processed data is shown in Fig. 10h.

4 Results

The proposed single camera unit based 3D imaging technique measured the round geometry sample under laboratory conditions. The sample has a thickness of 1.20 mm and a radius of 7.50 mm. The 3D point cloud map of the image reconstruction along with the central horizontal linear scan results are shown in Figs. 11 and 12. A similar pattern

was observed at the center of the linear line. The ability to extract the surface feature on the target was validated by the experimental results.

The 3D point cloud map was drawn to validate the reconstruction performance. The mean value of the detected thickness obtained by different methods is shown in Table 2. Compared with the laser displacement sensor result, the measured thickness from both experiments was accurate with a relative error of less than 3%, as shown in Fig. 12. The larger error in method 2 could be caused by the motion error of the robot arm, which can increase the multi-axis motion error during scanning. In addition, the feature profiles were measured using method #1 without the background pattern and using a conventional two-camera imaging system. The output of the laser displacement sensor was considered as baseline data. The average thickness measured by method #1 and conventional stereoscopy was 0.10 mm and 0.02 mm higher than the baseline data, respectively. From these experimental results, it was confirmed that method #1 with a single camera system, target scanning unit, and background pattern to reduce disparity error can be used for 3D surface imaging.

The experimental results showed that the single camera unit-based 3D imaging technique can provide a complete image reconstruction map. We increase the surface complexity, especially for the irregular ravines. A matte black metal logo of Texas A&M University was selected to validate the ability of surface feature extraction performance. The 3D reconstruction process follows the same principle as the cylindrical sample. The 3D point cloud map of the image reconstruction results is shown in Fig. 13.

Fig. 13 shows that the 3D results obtained by method #1 can represent the shape of the target sample, indicating that the proposed method can perform accurate measurements of samples with complicated geometries. However, in method #2, there may be misalignment and motion error of the robot arm, which may also cause tilt error, making the whole structure appear to be tilted.

5 Error Analysis

In the following, we will introduce physical and mathematical compensation to mitigate the effects of motion error on 3D reconstruction accuracy.

5.1 Tilt Error

For a stereoscopic imaging system, the angle of the target and the camera should ideally be identical during calibration and measurement. Subtle angular transformations between the target and the camera can cause errors in the disparity calculation, resulting in failure of the



Fig. 10 3D image reconstruction process: results

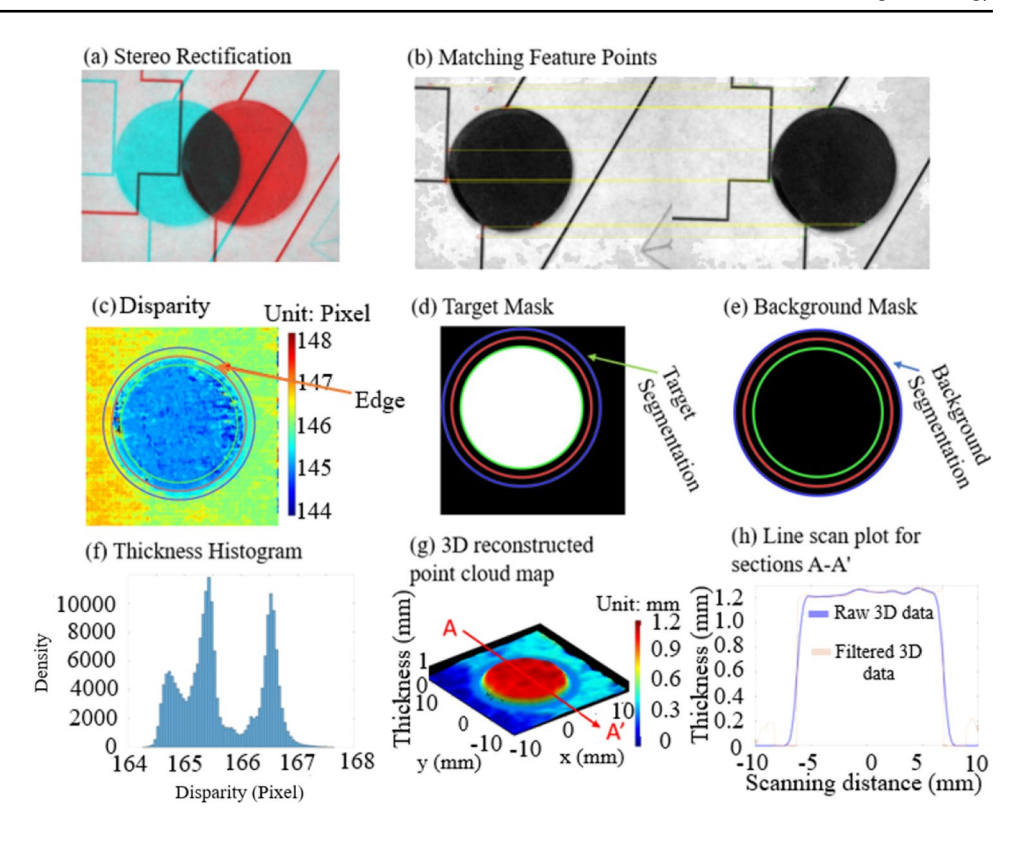


Fig. 11 3D image reconstruction point cloud results: (a) Method #1 and (b) Method #2

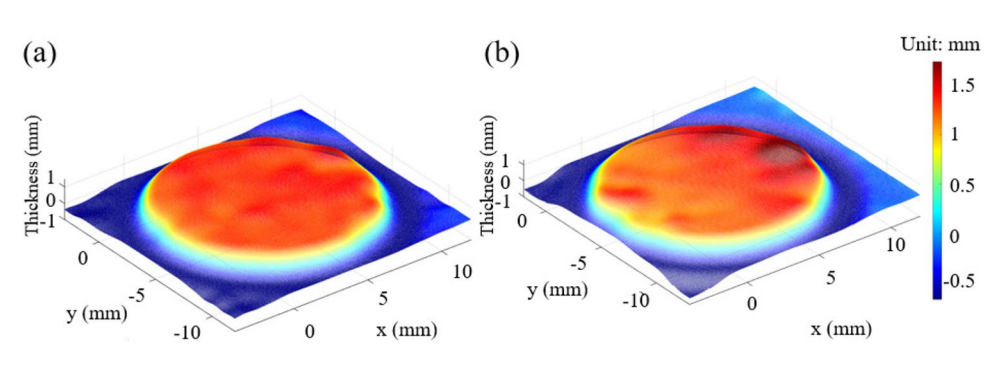
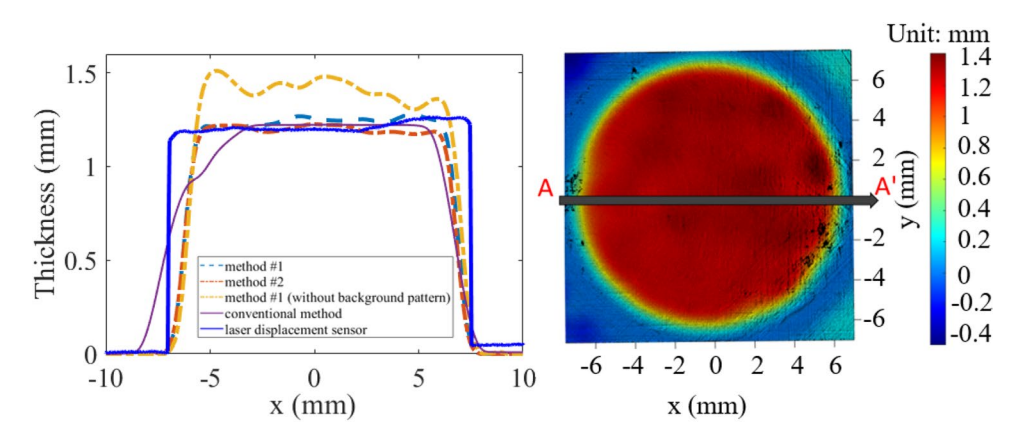


Fig. 12 Experimental result: 3D image and its line profiles obtained by several methods



3D reconstruction. In traditional cases, we are forced to adjust the position of the camera and recalibrate the camera system. Take advantage of the multi-axis freedom

of the robot manipulator. We can change the robot's pose so that the camera and the target can regain the angle of the original calibration.



Table 2 Comparison of line scan results: Profile A-A' in Fig. 12

	Method #1	Method #2	Method #1 (no back- ground pattern)	Conventional method	Laser dis- placement sensor
Averaged thick-ness	1.20 mm	1.24 mm	1.30 mm	1.22 mm	1.20 mm

The "Roosevelt" design of the United States 10-cent coin was chosen as a test sample. First, the sample was mounted on a goniometer stage at an angle of 25 degrees and the stereo image was captured in its original position. Second, a robot was used to tilt the camera 25 degrees so that the camera and target were in a vertical position (Fig. 14).

Comparing the two disparity maps above, we can clearly see that when the calibration and measurement angles change, the quality of the disparity map decreases. However, if we use the robot to compensate for its tilt error, we can obtain an accurate disparity map. Using a robot, the camera system was able to measure a thickness of about 1.30 mm. compared to the coin specifications of 1.35 mm. The thickness discrepancy was only 3.70% and the disparity map clearly shows the head of President Roosevelt on the coin. For reference, the blue areas in Figure 14c are caused by the highly reflective areas where the thickness calculation result may have a large error with the

true value, whose thickness is assigned as an unrepresentable value or known as Not a Number (NaN) by filter processing to ensure the accuracy of the overall thickness calculation.

5.2 Baseline Error

Ideally, the baseline distance should be consistent when performing camera calibration. (B_c) and actual measurement (B_m) . When $B_c = B_m$. We can define the measured thickness as the true value. (Z_t) , assuming no measurement error and no calculation error during the measurement process. In many cases, camera setup and baseline in complex industrial environments are affected by many uncontrollable factors that may not be able to be calibrated to the ideal baseline length. Also, the Pose Repeatability (RP) and Pose Accuracy (AP) of the robot manipulator are affected by both kinematic error and non-kinematic error, etc. Therefore, in actual applications cases, the measured thickness (Z_m) and the true thickness (Z_t) are not identical due to the baseline error.

According to Equation 1 and the measurement method above. The disparity has a proportional relationship with the baseline distance based on triangulation.

$$\frac{B_c}{d_c} = \frac{B_m}{d_m} \tag{5}$$

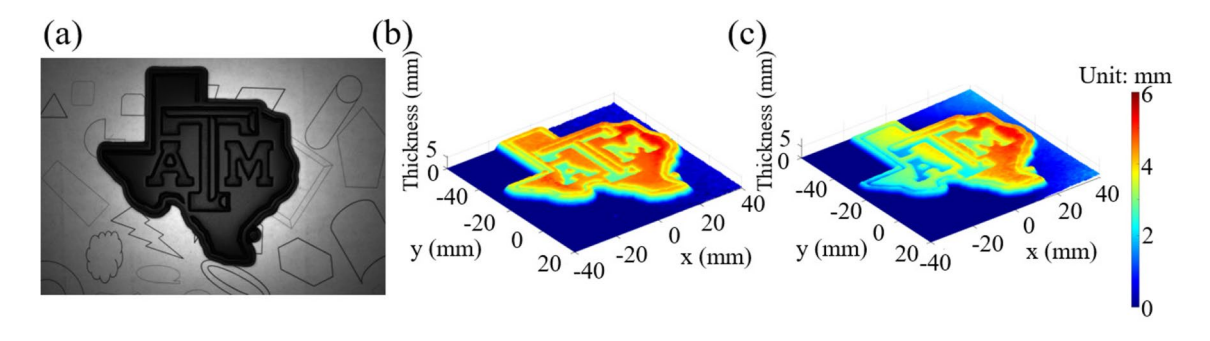
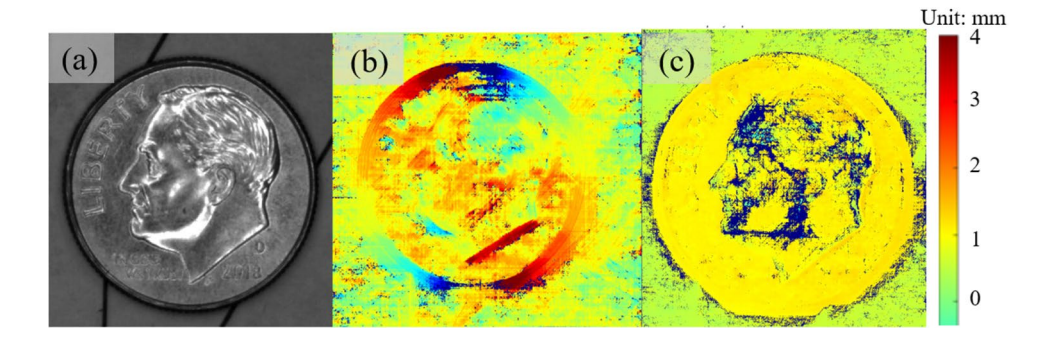


Fig. 13 3D reconstruction point cloud results: (a) camera view image of the target, (b) method #1, and (c) method #2

Fig. 14 3D image reconstruction results: (a) Original image and (b) Disparity maps without tilt compensation and (c) Disparity maps with tilt error compensation





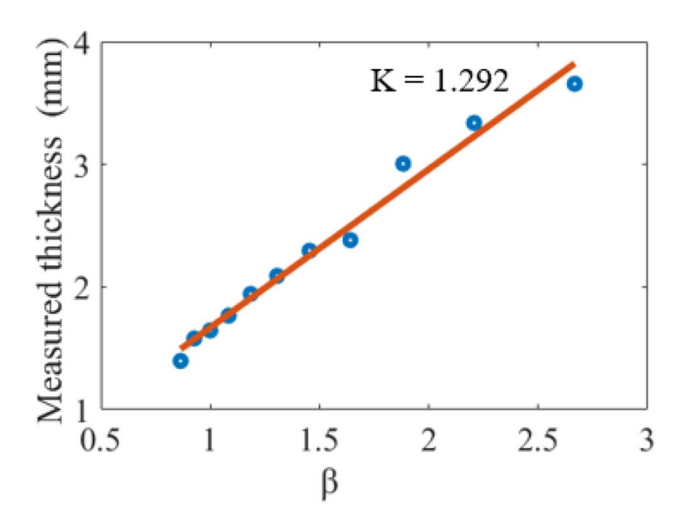


Fig. 15 Experimental result: curve chart of measured thickness versus β

Where d_c is the disparity between two images during camera calibration and m is the disparity between two images during the actual measurement.

Based on the above relationship, the equation for the measured thickness can be rewritten as follows:

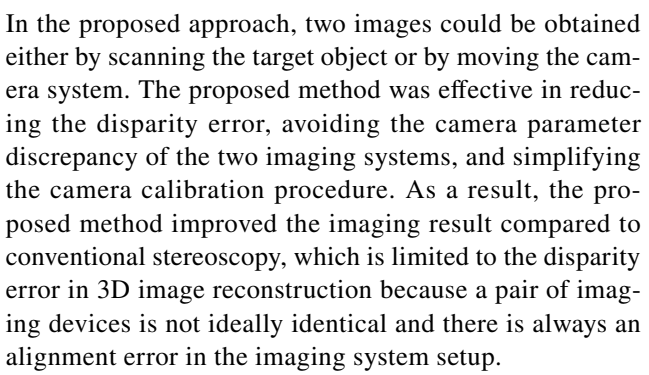
$$Z_{m} = \frac{B_{c}f}{d_{m}} = \frac{B_{c}f}{\frac{B_{m}}{B_{m}}d_{c}} = \frac{B_{c}}{B_{m}}Z_{t} = \beta Z_{t}$$
(6)

The above equation indicates that there is a positive relationship between Z_m and β . To verify this theory, the target with a thickness of 1.65 mm and a radius of 7.50 mm was selected as the reference for this experiment. The camera system was calibrated at a baseline of 8.0 mm. Ten groups of stereo images were collected at a constant rate of change of 0.625 mm in baseline distance (Fig. 15).

The above graph shows that the relationship between β and the measured thickness variation (Z_m .) is controllable and we can obtain the ratio of the regression sum of squares (SSR) and the total sum of squares (SST) equal to 0.9814. This experiment verifies the linear relationship between β and Z_m . The experiment shows that when using single camera system, even if the baseline length of the calibration and the baseline length during measurement are different, the true thickness of the measured target can still be recovered by using Equation 6.

6 Conclusion

The single camera-based stereoscopy was developed and preliminarily validated with the sample test. Successful 3D surface imaging was achieved by 3D image reconstruction from a pair of images obtained either from two different camera positions or from two different target positions.



For future work, the proposed method will be implemented for 3D imaging of the rotating object, employing strobo-stereoscopy, for in-process roll pattern and cutting tool geometry inspection.

Acknowledgements The research team thanks Honeywell Federal Manufacturing & Technologies LLC for the project (DE-NA0002839) and National Science Foundation for the project (CMMI #2124999).

Authors contribution All authors contributed equally to this work.

Data availability The data that supports the findings of this study are available from the corresponding author upon reasonable request.

Declarations

Disclosures The authors declare no conflicts of interest.

References

- Varda, K., Zaimović-Uzunović, N., Softić, A., & Bešlagić, E. Dimensional and Shape Control of the Part Using Cmm and 3d Scanner. Available at SSRN 4298597.
- Ito S, Tsutsumi D, Kamiya K, Matsumoto K, Kawasegi N (2020) Measurement of form error of a probe tip ball for coordinate measuring machine (CMM) using a rotating reference sphere. Precis Eng 61:41–47
- Fan KC, Li RJ, Xu P (2019) Design and verification of micro/ nano-probes for coordinate measuring machines. Nanomanuf Metrol 2(1):1-15
- Li S, Zeng L, Feng P, Yu D (2020) An accurate probe pre-travel error compensation model for five-axis on-machine inspection system. Precis Eng 62:256–264
- Edmondson V, Woodward J, Lim M, Kane M, Martin J, Shyha I (2019) Improved non-contact 3D field and processing techniques to achieve macrotexture characterization of pavements. Constr Build Mater 227:116693
- Virtanen JP, Daniel S, Turppa T, Zhu L, Julin A, Hyyppä H, Hyyppä J (2020) Interactive dense point clouds in a game engine. ISPRS J Photogramm Remote Sens 163:375–389
- Lozano A, Hayes JC, Compton LM, Azarnoosh J, Hassanipour F (2020) Determining the thermal characteristics of breast cancer based on high-resolution infrared imaging, 3D breast scans, and magnetic resonance imaging. Sci Rep 10(1):1–14
- Kolose S, Stewart T, Hume P, Tomkinson GR (2021) Prediction of military combat clothing size using decision trees and 3D body scan data. Appl Ergon 95:103435



- Huang C, Wang G, Song H, Li R, Zhang H (2022) Rapid surface defects detection in wire and arc additive manufacturing based on laser profilometer. Measurement 189:110503
- Cui B, Tao W, Zhao H (2021) High-precision 3d reconstruction for small-to-medium-sized objects utilizing line-structured light scanning: A review. Remote Sens 13(21):4457
- Yang SP, Seo YH, Kim JB, Kim H, Jeong KH (2019) Optical MEMS devices for compact 3D surface imaging cameras. Micro Nano Syst Lett 7:1–9
- Song Z, Song Z, Zhao J, Gu F (2020) Micrometer-level 3D measurement techniques in complex scenes based on stripe-structured light and photometric stereo. Opt Express 28(22):32978–33001
- Li C, Yu L, Fei S (2019) Real-time 3D motion tracking and reconstruction system using camera and IMU sensors. IEEE Sens J 19(15):6460–6466
- Lee CB, Guo X (2022) Spatially Resolved Stereoscopic Surface Profiling by using a Feature-Selective Segmentation and Merging Technique. Surf Topogr: Metrol Prop 10:014002
- Xiangyu Guo and ChaBum Lee (2022) Fluorescence Strobo-Stereoscopy for Specular Reflection-Suppressed Full Field of View Imaging. Measurement 192:11090
- Guo X, Lee CB (2021) Preliminary study of phase-shifting strobo-stereoscopy for cutting tool monitoring. J Manuf Process 64:1214–1222
- He K, Sui C, Lyu C, Wang Z, Liu Y (2020) 3D reconstruction of objects with occlusion and surface reflection using a dual monocular structured light system. Appl Opt 59(29):9259–9271
- Lyu C, Li P, Wang D, Yang S, Lai Y, Sui C (2020) High-speed optical 3D measurement sensor for industrial application. IEEE Sens J 21(10):11253–11261
- Ye J, Zhou C (2021) Time-resolved coded structured light for 3D measurement. Microw Opt Technol Lett 63(1):5–12
- Bao Y, Tang L, Srinivasan S, Schnable PS (2019) Field-based architectural traits characterisation of maize plant using time-offlight 3D imaging. Biosyst Eng 178:86–101
- Altuntas C (2021) Triangulation and time-of-flight based 3D digitisation techniques of cultural heritage structures. Int Arch Photogramm Remote Sens Spat Inf Sci 43:825–830
- Jiang Y, Karpf S, Jalali B (2020) Time-stretch LiDAR as a spectrally scanned time-of-flight ranging camera. Nat Photonics 14(1):14–18
- Pahl T, Hagemeier S, Künne M, Yang D, Lehmann P (2020) 3D modeling of coherence scanning interferometry on 2D surfaces using FEM. Opt Express 28(26):39807–39826

- 24. Wu Y, Luo Y, Chaudhari G, Rivenson Y, Calis A, de Haan K, Ozcan A (2019) Bright-field holography: cross-modality deep learning enables snapshot 3D imaging with bright-field contrast using a single hologram. Light: Sci Appl 8(1):25
- 25. Henseler H, Khambay BS, Bowman A, Smith J, Siebert JP, Oehler S et al (2011) Investigation into accuracy and reproducibility of a 3D breast imaging system using multiple stereo cameras. J Plast Reconstr Aesthet Surg 64(5):577–582
- Cadena C, Gálvez-López D, Ramos F, Tardós JD, Neira J (2010) Robust place recognition with stereo cameras. In: 2010 IEEE/ RSJ International Conference on Intelligent Robots and Systems. IEEE, pp 5182–5189
- Yang S, Gao Y, Liu Z, Zhang G (2020) A calibration method for binocular stereo vision sensor with short-baseline based on 3D flexible control field. Opt Lasers Eng 124:105817
- Kim BH, Khan D, Choi W, Kim MY (2019) Real-time counter-UAV system for long distance small drones using double pantilt scan laser radar. In: Laser radar technology and applications XXIV, vol 11005. SPIE, pp 80–86
- Rapp J, Tachella J, Altmann Y, McLaughlin S, Goyal VK (2020) Advances in single-photon lidar for autonomous vehicles: Working principles, challenges, and recent advances. IEEE Signal Process Mag 37(4):62–71
- Fan M, Liu Y (2022) Image processing technology based on computer vision algorithm. In: 2022 4th International Conference on Artificial Intelligence and Advanced Manufacturing (AIAM). IEEE, pp 847–850
- 31. Burger W (2016) Zhang's camera calibration algorithm: indepth tutorial and implementation, vol HGB16-05. University of Applied Sciences Upper Austria, Hagenberg, Austria, pp 1–6

Publisher's note Springer Nature remains neutral with regard to jurisdictional claims in published maps and institutional affiliations.

Springer Nature or its licensor (e.g. a society or other partner) holds exclusive rights to this article under a publishing agreement with the author(s) or other rightsholder(s); author self-archiving of the accepted manuscript version of this article is solely governed by the terms of such publishing agreement and applicable law.

